Joule

CellPress
OPEN ACCESS

Article

Quantifying multiphase SEI growth in sulfide solid electrolytes

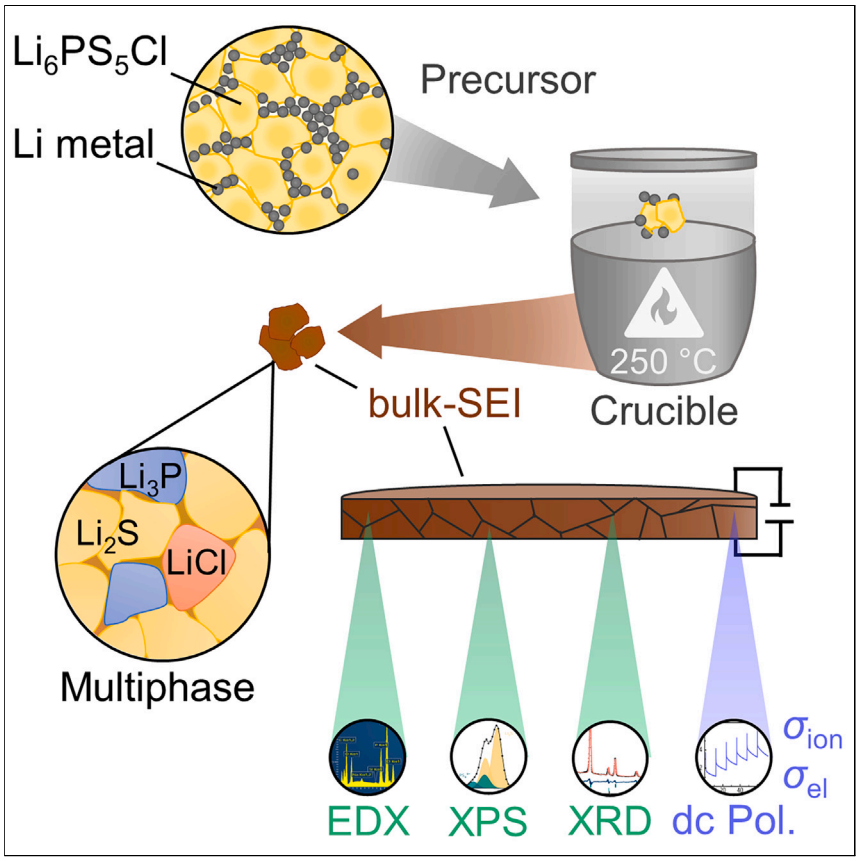

The incorporation of lithium metal anodes could increase the energy density of solid-state batteries, potentially surpassing that of lithium-ion batteries. However, this is hindered by the chemical reduction of solid sulfide electrolytes in contact with lithium metal. The objective of this study is to better understand the transport properties of typical multiphase SEIs, providing quantitative design guidelines for stabilizing the Li|solid electrolyte interface and its kinetics.

Christoph D. Alt, Nadia U.C.B. Müller, Luise M. Riegger, Burak Aktekin, Philip Minnmann, Klaus Peppler, Jürgen Janek

juergen.janek@pc.jlug.de

Highlights

A transferable approach simulated the degradation of sulfide solid electrolytes

dc polarization reveals the ionic and electronic conductivity of bulk-SEI material

Using the Wagner-type diffusion model, SEI growth kinetics is evaluated

Quantitative design guidelines are given to attain sufficient long-term stability

Alt et al., Joule *8*, 2755–2776
October 16, 2024
Published by Elsevier Inc.
https://doi.org/10.1016/j.joule.2024.07.006

Joule

CellPress
OPEN ACCESS

Article

Quantifying multiphase SEI growth in sulfide solid electrolytes

Christoph D. Alt,[1,2] Nadia U.C.B. Müller,[1,2] Luise M. Riegger,[1,2] Burak Aktekin,[1,2] Philip Minnmann,[1,2] Klaus Peppler,[1,2] and Jürgen Janek[1,2,3,*]

SUMMARY

The incorporation of lithium metal anodes in solid-state batteries (SSBs) is impeded due to the chemical reduction of sulfide solid electrolytes (SEs) in contact with lithium metal. Growth mode, composition, and microstructure of a few model-type SE interphases (SEIs) are slowly unveiled. The objective of this study is to better understand the transport properties of typical multiphase SEIs by direct reaction of the SE with lithium metal powder. Hence, the composition and conduction properties (σ_{ion} and σ_{el}) of synthesized bulk-scale SEI-type material (of Li_6PS_5Cl) are analyzed. The kinetic predictions using a Wagner-type diffusion model align well with recent results of electrochemical studies on cell-level multiphase SEIs. Accordingly, these findings enhance the ability to model transport parameters with greater accuracy and contribute to a deeper understanding of SEI growth and kinetics in SSBs. The need to stabilize the Li|SE interface by controlling the partial conductivities of the resulting SEI is emphasized.

INTRODUCTION

In the ongoing transition toward sustainable electric transportation, solid-state batteries (SSBs) are being recognized as a promising advancement of conventional lithium-ion batteries (LIBs).[1–3] SSBs often utilize solid electrolytes (SEs) that replace flammable liquid organic electrolytes of LIBs, potentially ensuring the safe operation of the system.[4–6] Among the multitude of lithium-ion-conducting materials, lithium thiophosphate-based SEs, such as lithium argyrodites Li_6PS_5X (X = Cl, Br, I), have garnered significant attention from both academia and industry. They are considered suitable to be employed in SSBs for being highly conductive (up to 20 mS cm^{-1}),[7,8] and reasonably malleable to form sufficient interfacial contacts. Integrating lithium metal anodes (LMAs) in SSBs, which is not feasible in LIBs due to the significant dendrite risk, is expected to boost their energy and power densities.[9–12]

As for all electrochemical cells, the performance of SSBs relies on the interplay of the negative electrode (often addressed as anode), separator electrolyte, and positive electrode (often addressed as cathode).[13,14] The SE separates the electrodes and allows ion transport while preventing electronic conduction. Due to their very low (anode) and very high (cathode) potentials, the electrodes can either reduce or oxidize the SE at the corresponding interface, which poses stability issues. Based on thermodynamic data, Zhu et al.[15] and Richards et al.[16] computed the (onset) potentials for reduction and oxidation, along with the resulting equilibrium phases. In particular, the stabilization of Li|SE interfaces is a major challenge in the development of lithium thiophosphate-based SSBs if no other stable separator SE is being

CONTEXT & SCALE

Lithium-ion batteries (LIBs) are approaching physicochemical limits in terms of energy density and fast-charging capability. To meet the demands of future (mobile) applications, the integration of lithium metal anodes in solid-state batteries holds the potential to enable high-performance storage beyond LIBs. However, morphological changes during operation and degradation of (sulfide) solid electrolytes in contact with lithium metal are unsolved issues, both of which are closely interconnected.

To enable lithium metal solid-state batteries, it is crucial to control and optimize the lithium|solid electrolyte interface. This study provides new insight into the characteristics and growth kinetics of the resulting interlayer through a direct reaction of sulfide solid electrolyte with lithium metal powder. Our findings highlight the importance of controlling the partial conductivities of the resultant multiphase layer to stabilize the metal anode. Quantitative design guidelines are derived.

used (like garnet-type SE).[17,18] When in contact with lithium metal, which exhibits the lowest possible redox potential (i.e., $E_H[Li^+/Li] = -3.04$ V vs. SHE), ternary and higher thiophosphate SEs are thermodynamically unstable. In the case of lithium argyrodites, they are reduced and decomposed to binary lithium compounds, as described in Equation 1.[15,19] These binary decomposition products are thermodynamically stable against lithium metal, and thus, local equilibrium (with lithium metal) will be established. Essentially, P(+5) is reduced to P(−3) and other low-valent phosphorous species,[15] which drive the reaction along with the formation of highly stable Li_2S and LiCl (for the sake of simplicity, the formation of stoichiometric Li_3P is assumed in the following):

$$Li_6PS_5X + 8\,Li^0 \rightarrow 5\,Li_2S + Li_3P + LiX \text{ with } X = Cl, Br, I \qquad \text{(Equation 1)}$$

During this (chemical) degradation, a multiphase reaction layer is formed. The morphological stability and growth of this interphase are determined by its transport properties.[20,21] Assuming a classical diffusion-controlled solid-state reaction, the persistent degradation of sulfide SEs can only be stopped once sufficiently strong counter-acting forces compensate the chemical driving force or if a product is somehow accumulated such that the kinetics is slowed down to a virtually zero rate. As some of the interphase components like lithium halides and lithium phosphide show lithium-ion conductivity—even if it is low—it is expected that the electronic conductivity within the degradation layer will define the interphase growth rate. Two types of interphases have been defined and reported[21]: (1) mixed ion/electron-conducting interphases (MCIs), which grow more or less continuously due to both high ionic and electronic partial conductivity[22] and eventually cause short circuiting of SSBs, and (2) predominantly ion-conducting interphases with negligible partial electronic conductivity. Consequently, the latter are denoted SE interphases (SEIs) in line with the analog interphase in liquid electrolytes.[23–25] They are assumed to show a square-root of time growth behavior in the ideal case, which can be described by a Wagner-type model.[19,26] We like to highlight already at this early stage that a purely diffusion-controlled SEI formation will theoretically not come to a rest but will get slowed down with time.

Hence, for Li_6PS_5Cl (and other thiophosphate SEs), Wenzel et al.[19] and Riegger et al.[27] observed that the SEI growth (in contact with lithium foil) persisted for several hours to days with a significant slowdown in growth. In experiments based on a novel electrochemical titration technique, Aktekin et al.[28] further described a square-root of time relationship for the SEI growth in anode-free cells (i.e., for freshly deposited lithium). These findings imply that the electronic conductivity of the formed SEI is too high to effectively suppress continuous growth. On the contrary, Otto et al.[29] reported that the degradation reaction of Li_6PS_5Cl with vapor-deposited lithium exhibited self-limiting kinetics, ultimately resulting in a layered SEI microstructure. This disagreement on the long-term SEI growth highlights the importance of gaining a better understanding of SEI conduction characteristics with respect to SEI growth. In view of the great relevance of this SEI for the future of sulfide-based SSBs, the unclear understanding is not satisfying.

SEIs show completely differing chemical, structural, and mechanical properties compared with pristine sulfide SEs, mainly due to the multiphase composite character and the negative volume change during growth relative to the SE itself.[30] Hence, various effects occur such as interface cracking and pore formation, loss of accessible lithium, and hampered lithium-ion transfer.[13,20] As a result of the additional SEI layer, the charge transfer resistance at the interface between lithium metal and the SE is typically increased. By destroying the SE structure, the SEI formation

[1]Institute of Physical Chemistry, Justus Liebig University, Heinrich Buff Ring 17, 35392 Giessen, Germany

[2]Center for Materials Research, Justus Liebig University, Heinrich Buff Ring 16, 35392 Giessen, Germany

[3]Lead contact

*Correspondence: juergen.janek@pc.jlug.de

https://doi.org/10.1016/j.joule.2024.07.006

has a detrimental impact on full cell level, supporting dendrite formation and a corresponding decrease in cycle life.[30,31] Hence, the presence of a SEI has a significant impact on the fundamental characteristics and long-term performance of SSBs, which several approaches aim to inhibit.[32–34] Eventually, controlled degradation,[35–37] and stabilized Li|SE interfaces,[38] while supporting sufficient ionic conductivity and reduced SEI impedance, may enable the commercialization of SSBs.

Despite their critical role, studies on the electrical and microstructural properties of SEIs are scarce due to the lack of suitable methods (i.e., due to limited spatial resolution and difficulties in sample preparation). Examining the SEI presents challenges because of its nanoscale nature and the concealed (buried) interface. Hence, investigations are mostly limited to surface sensitive characterization techniques,[21,29,39] electron microscopy,[40,41] or electrochemical impedance spectroscopy.[27,42] Other properties of SEIs are typically approximated to mirror the characteristics of their constituent (bulk) phases, despite limited understanding of their individual distribution and nature in complex SEI layers. On one side, there is a lack of experimental evidence regarding the composite structure of multiphase SEI layers and the widely acknowledged presumption of electronically insulating characteristics. On the other side, there is little experimental research on these individual phases in battery-relevant contexts, specifically concerning partial ionic and electronic transport properties. Hence, establishing correlations between assumptions about the SEI layer, validating experimental results, and interpreting electrochemical data is a complex task.

In this study, we introduce a novel approach to gain deeper comprehension of the multiphase SEI layer at a new scale. Li_6PS_5Cl (LPSCl) as model SE is utilized to investigate the SEI properties of sulfide SEs in contact with lithium metal. We synthesize bulk-phase SEI-type material ("bulk-SEI") through direct synthesis from LPSCl and micron-size lithium metal powder. This enables the assessment of various SEI properties without the need for approximation based on individual constituent phases. X-ray powder diffraction (XRD) and X-ray photoelectron spectroscopy (XPS) measurements are conducted to confirm the successful synthesis of the bulk-SEI and validate the chemical composition. The morphology of the synthesized bulk-SEI particles is examined using scanning electron microscopy (SEM). The presence of domains enriched in S, P, or Cl is confirmed by complementary energy dispersive X-ray spectroscopy (EDX). dc polarization under selectively blocking conditions, i.e., the Wagner-Hebb configuration,[43,44] is utilized for electrochemical characterization. Thereby, we quantify the partial ionic and electronic conductivities of the synthesized multiphase bulk-SEI. Based on these data, we assess SEI growth as well as its thickness using a Wagner-type diffusion model, which is in very good agreement with electrochemical studies on cell-level multiphase SEIs, and discuss its effect on SSBs. The findings from these studies provide a comprehensive and holistic understanding of the nanoscale SEI characteristics. Ultimately, we establish a guideline by estimating suitable partial conductivities for the SEI to optimize the Li|LPSCl interface and achieve sufficient long-term stability.

RESULTS AND DISCUSSION

To be a suitable separator material to incorporate LMAs and commercialize SSBs, a (sulfide) SE must fulfill various criteria, including high ionic conductivity. In the case of lithium thiophosphate-based SSBs, the challenges posed by the evolution and growth of multiphase SEIs result in increased ionic resistance and require further investigation.

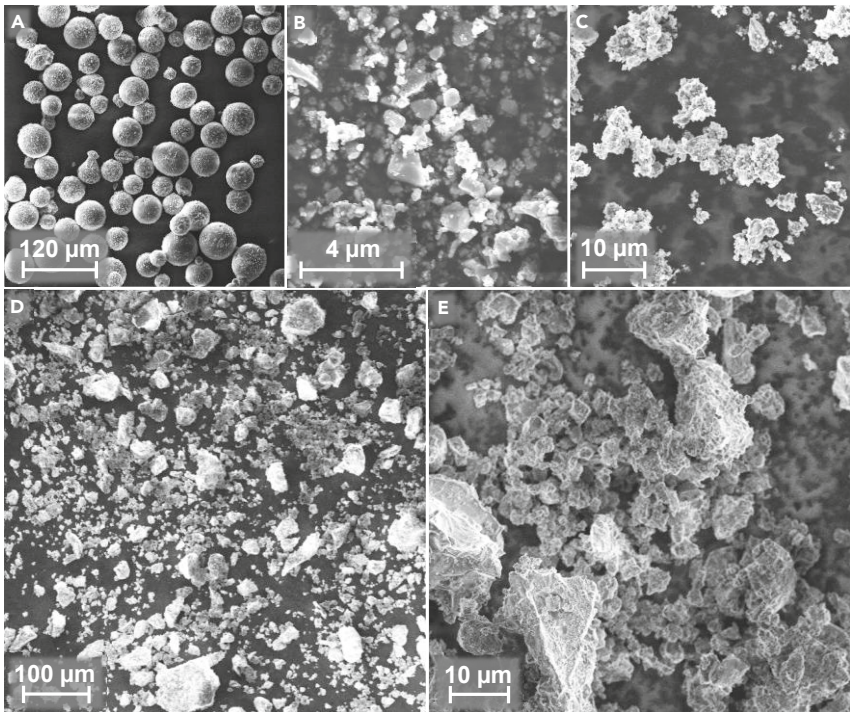

Figure 1. Scanning electron microscope images of the starting materials and the synthesized bulk-SEI

(A–C) Lithium metal powder (A), LPSCl powder (B), and the homogeneous mixture of both materials (hand-ground, serving as precursor) (C).

(D and E) Image of the synthesized bulk-SEI particles after annealing at 250°C and subsequent hand grinding in the mortar are shown in (D) and (E). No remains of spherical lithium metal powder have been identified. The particle size appears to be significantly increased, while differences in shape to the initial LPSCl and untreated mixture are found.

Material synthesis and chemical analysis of multiphase bulk-SEI

Detailed information on the prepared lithium metal powder is given in the supplemental information. This includes SEM images of single particles and the particle size distribution (Figures S1 and S2; Section A) and XRD results (Figure S4; Section C). Moreover, Figure S9 (Section D) presents the XPS depth-profiling results of lithium metal particles, which reveal the passivation layer comprising lithium hydroxide, Li_2O, lithium carbonate, and carbon species.

In Figure 1, SEM images of the starting materials are compared: freshly prepared lithium metal powder (A), LPSCl powder (B), and their hand-ground mixture before annealing (C). XRD analysis of the mixture (Figure S6; Section C, supplemental information) did solely disclose minor signs of reaction (as evidenced by clear LPSCl and lithium metal reflections), and electrochemical testing revealed high electronic conductivity—even after few weeks of storage. Hence, it was employed as precursor in the subsequent heat treatment process at 250°C. Please note that this is an extra (synthesis) step, which may lead to unavoidable deviations from the characteristics (i.e., morphology and properties) of the actual SEI in SSBs. Images of the resulting bulk-SEI particles (Figures 1D and 1E, at different magnifications) provide first insights into their morphology. It comprises micron-sized, agglomerated secondary particles with various shapes and sizes. The absence of spherical particles (i.e., lithium metal powder) in the precursor (C) and the final product (D and E) provides an initial indication of the successful mixing and subsequent reaction, respectively.

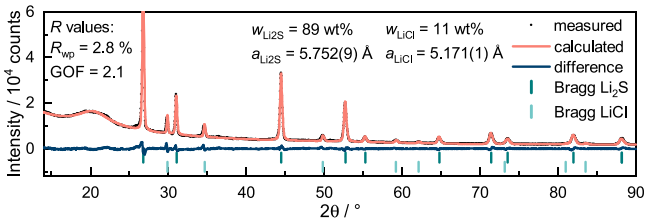

Figure 2. Representative X-ray diffraction pattern of the synthesized bulk-SEI and the corresponding Rietveld refinements

Single phases of Li_2S (ICSD: 196932) and LiCl (ICSD: 52235) are identified. *w*, *a*, R_{wp}, and GOF are the mass fraction, lattice constant, weighted profile R-factor, and goodness of fit, respectively.

The particle size of the product appears even after consecutive grinding to be increased compared to the initial particle size of the sulfide SE and the precursor mixture. As mentioned above, the increased particle size could be related to the annealing step. Additional SEM images with further details on the bulk-SEI's morphology are shown in Figure S3; Section B, supplemental information.

The properties of the synthesized bulk-SEI are notably responsive to the carefully measured stoichiometric ratio of reactants. Specifically, residuals of LPSCl may impact the partial ionic conductivity, while lithium metal residuals may affect the electronic conductivity. If residuals persist, we anticipate the latter to have a more significant impact. To avoid this, we adjusted the amounts of lithium metal powder and LPSCl to their corresponding molar ratio without risking an over-stoichiometric amount of lithium metal. Thus, to confirm the successful synthesis, ensure the absence of any remaining reactants, and acquire further information about the crystalline nature of the obtained bulk-SEI, phase analysis by means of powder XRD was performed (see Figure 2). While the interfering background in the 2θ range of 17°–23° is caused by the polyimide cover, the XRD pattern reveals distinct reflections corresponding to single phases of Li_2S and LiCl. Identifying both compounds indicates the (partially) successful synthesis according to the chemical reaction (Equation 1).

However, no traces of the expected Li_3P or any related phosphorous compounds, including intermediates, are detected via XRD. The most prominent reflections of phase-pure Li_3P occur at 23.4°, 24.0°, 26.8°, 42.3°, and 43.4° (ICSD: 26880). However, the detection of Li_3P is hindered by the polyimide cover, particularly up to 24°, and the Li_3P reflection at 26.8° superimposes with the most prominent peak of Li_2S. Additionally, no clear reflections are observed at 42.3° and 43.4°. Figure S7 (Section C, supplemental information) provides the magnified XRD pattern in the range of 40° to 62°.

The potential presence of multiple lithiated phosphorus compounds (e.g., Li_xP intermediates) significantly reduces the probability of their detection in the bulk-SEI due to the low fractions of each phosphorus compound. Moreover, another possible reason is the increased reactivity of Li_3P to moisture, with the polyimide covers used here only minimizing exposure to air. To the best of our knowledge, the observation of Li_3P in SEI studies has only been reported but remains challenging under ultra-high vacuum (UHV) conditions (e.g., by XPS).[45,46] Lastly, Li_3P may be in an amorphous (non-crystalline) state in the bulk-SEI, which is also often assumed in studies of phosphorus as an electrode material in batteries.[47–49]

The Rietveld refinement of the XRD pattern provides lattice constant values of *a* = 5.753 Å for the Li_2S phase and *a* = 5.171 Å for the LiCl phase, which are in good

agreement with previously reported values.[50,51] Furthermore, the refinement process reveals the mass fractions of the synthesized bulk-SEI for each identified compound. Li_2S represents the predominant fraction at 89 wt %, while LiCl accounts for only 11 wt % of the overall composition. It should be noted that the starting LPSCl material used in the synthesis already contained 3 wt % of LiCl as an impurity (identified by XRD refinement; see Figure S5; Section C, supplemental information). However, a direct comparison of these mass fractions obtained through XRD measurements to the expected values (of chemical reaction [Equation 1]) is not feasible due to the potential presence of unidentified or non-crystalline phases.

Notably, reflections of the initial constituents (lithium metal and LPSCl) are neither detected nor identified, especially in comparison with reference diffractograms of both materials and the precursor (see Figures S4–S6; Section C, supplemental information). Therefore, Figure S8 (Section C, supplemental information) provides a comparison of XRD patterns (raw data) between LPSCl, precursor mixture, and synthesized bulk-SEI. As mentioned above, we intentionally avoided using over-stoichiometric amounts of lithium metal during preparation. Hence, we did not aim to compensate for lithium loss originating from passivation films present on lithium metal powders. In addition, we believe that lithium metal powder would further be subjected to passivation during grinding and synthesis due to its high reactivity and increased surface area (even under inert conditions in gloveboxes). Therefore, some lithium metal is inevitably consumed due to passivation reactions (e.g., Li_2O, lithium hydroxide, and lithium carbonate formation), making it more likely for residual LPSCl to be present in the bulk-SEI. Additional lithium compounds, such as lithium hydroxide and Li_2O, are also not identified. With respect to residual LPSCl, there is a slight increase in intensity at ~36.5°. However, despite this observation, the primary (most prominent) reflections of LPSCl at 25.6°, 30.0°, and 31.5° are not detected for the bulk-SEI. We believe that these features are not conclusive for the presence of lithium metal or LPSCl residuals. Thus, we assume that residual amounts of either lithium metal or LPSCl are sufficiently small, distributed within the multiphase SEI, and passivated or isolated so that they do not affect the properties of the bulk-SEI, as will be discussed in the next section.

In order to gain additional chemical information, resolve the unidentified, missing, or amorphous phases, and provide a thorough understanding of the chemical composition of the bulk-SEI, a chemical analysis using XPS was carried out next. Furthermore, we conduct additional analysis to verify the absence of lithium metal traces within the bulk-SEI and to quantify any residual amounts of LPSCl that may not have been fully consumed. This is crucial to ensure that the properties of the bulk-SEI remain uncompromised.

Figure 3 shows the Li 1s, S 2p, and P 2p XP spectra of the synthesized bulk-SEI. No lithium metal signals at binding energies (BEs) below 53 eV and plasmon-loss features at ~60 eV are detected in the Li 1s spectrum. We also performed depth profiling, which did not provide additional information on the bulk-SEI structure or identify residual amounts of lithium metal (Figure S10; Section E, supplemental information). This is in contrast to the XP spectra of lithium metal powder (compare Figure S9; Section D, supplemental information). Hence, these results verify the prior findings and consequently validate the complete consumption of lithium metal. Please note that minor impurities of lithium hydroxide and carbonates (both at 55.4 eV) as well as Li_2O (54.5 eV) cannot be prevented—even at dynamic vacuum conditions during synthesis. This can be attributed to the highly reactive nature of lithium metal and its increased surface area in powder form. However, as crystalline

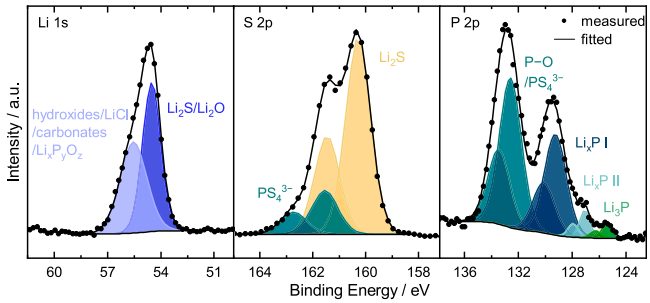

Figure 3. X-ray photoelectron Li 1s, P 2p, and S 2p spectra of the synthesized bulk-SEI

The analysis of these spectra revealed the successful synthesis of bulk-SEI. In the S 2p and P 2p spectra, the evolution of Li_2S and Li_3P (and related polyphosphides) is clearly evidenced, respectively. In the Li 1s spectra, it is evident that lithium metal is absent and has been entirely consumed. However, only minor residual amounts of LPSCl ($P–O/PS_4^{3-}$ doublets in the S 2p and P 2p spectra) may remain present, as confirmed by quantitative analysis (Figure S11).

impurities could not be identified by XRD measurements, we consider the impurity fractions to be negligible. XPS quantification (Figure S11; Section E, supplemental information) showed that the major impurities are lithium hydroxides resulting from reactions with trace amounts of moisture and oxygen and that the peak at 55.4 eV (in Li 1s) is mainly dominated by the Li_2S with smaller contributions of Li_2O. Both aspects are identified by comparing the quantification of the Li 1s with the O 1s and S 2p spectra, respectively. Unfortunately, signals of LiCl and (oxygenated) phosphorous species superimpose with those of lithium hydroxides.

The complete reduction of LPSCl to various decomposition products is evident in the S 2p and P 2p spectra. In the S 2p spectrum, the distinct signal at 160.3 eV can be assigned to Li_2S. This finding matches the thermodynamic predictions. Thus, Li_2S is formed during the reduction of LPSCl by lithium metal (as also confirmed by XRD). The prevalence of Li_2S is consistent with the chemical reaction (Equation 1), comprising the main volume fraction of the SEI (theoretically 71 vol % Li_2S).

In contrast to our XRD results, the P 2p spectrum shows indeed reduced phosphorus species in different lithiated (non-stoichiometric) states. While the signal of Li_3P at a BE of 125.4 eV can be clearly identified, two other well-separated doublets (127.1 and 129.3 eV, respectively) are detected, indicating lithium polyphosphides with slightly decreased lithium content (such as LiP_5, LiP_7, or Li_xP with $x < 3$). As these compounds are not detected in the XRD pattern, they are possibly in an amorphous state. Quantification results in Figure S11 (Section E, supplemental information) show that the total amount of phosphorous in the bulk-SEI is as expected. However, the identification of multiple species explains the lower-than-expected atomic fraction of Li_3P and the difficulties encountered in XRD analysis.

Depending on the XPS measurement conditions, it is common in SEI studies to detect low intensities of Li_3P as well as contributions (at higher intensities) of various phosphorous species (Li_xP).[19,45] Wenzel et al.[46] reported the high reactivity of Li_3P with trace amounts of oxygen and moisture inside the XPS chamber (i.e., UHV conditions), resulting in the consumption of freshly reduced Li_3P. This demonstrates that observation of Li_3P in SEI studies is still difficult, even under UHV conditions, and especially for XRD and other post mortem techniques.[28] To verify these challenges in the analysis of Li_3P, we synthesized samples of Li_3P (see supplemental experimental procedures, supplemental information). Our XPS study (Figure S14; Section F, supplemental information) shows large contributions from Li_xP and only minor

signals from Li_3P for the bulk-phase Li_3P reference sample, emphasizing the instability of Li_3P. Further, it has been reported that the availability and amount of lithium present during the SE degradation reaction are understood to affect the fraction of Li_3P.[45] Hence, the identification of three reduced phosphorous species may be attributed to regions with different lithium metal accessibilities in our synthesis reaction. Nonetheless, we believe that during the cycling of SSBs, there may also be variations in lithium availability influencing the growth of the SEI.

Similar to the S 2p spectrum (at 161.6 eV), the P 2p spectrum also shows signals of residual PS_4^{3-} species at 132.6 eV, also overlapping with those of oxygenated phosphorous species (P–O). The latter species are also identified in measurements of bulk-phase Li_3P (Figure S14; Section F, supplemental information), which are used as reference to identify the BE of P–O (between 132 and 134 eV). PS_4^{3-} signals potentially indicate that LPSCl is not entirely consumed and minor residuals may remain present in the obtained bulk-SEI material. Quantification results in Figure S11 (Section E, supplemental information), however, show that P–O contributes more significantly to the shared peak with PS_4^{3-}, highlighting the relatively low amount of residual LPSCl. This becomes evident by comparing the quantification of the S 2p spectra, which demonstrates the low contribution of PS_4^{3-} in P 2p as the atomic percentage for PS_4^{3-} in S 2p should be four times higher compared with P 2p. Since we could also not identify any remaining LPSCl by XRD measurements, we consider its residual quantity to be insignificant. Therefore, we assume that the properties of the bulk-SEI remain unaffected, and any potential residual amount of precursor is likely to be small and distributed within the bulk-SEI.

In the Cl 2p spectrum, the signal caused by LPSCl and LiCl exhibit similar BEs and cannot be distinguished. Therefore, it is not possible to analyze the reduction of LPSCl in the Cl 2p spectrum. However, the evolution of LiCl in the bulk-SEI by decomposition of LPSCl is clearly observed by XRD analysis. Furthermore, the O 1s spectrum, although not presented here, substantiates the development of lithium hydroxides and carbonates, Li_2O, and oxygenated phosphorous species (P−O). We emphasize that impurities such as Li_2O do not compromise the validity of our synthetic approach as Li_2O can form due to trace amounts of oxygen and moisture during storage, synthesis, or measurement.[52] The O 1s, C 1s, and Cl 2p spectra are presented in Figure S12 (Section E, supplemental information). XP spectra (for reference purposes) of pristine LPSCl are provided in Figure S15 (Section F, supplemental information).

Observing the evolution of Li_2S, Li_3P (and lithium polyphosphides), and LiCl by XPS and XRD, the successful synthesis of bulk-SEI is demonstrated. Combined XRD, XPS, and quantitative analysis provide assurance that the insignificant amounts of residual precursor material should not interfere with the accurate description and modeling of multiphase SEI properties in the synthesized bulk-SEI material. We note that, alongside the heat treatment, mechanochemical reactions taking place in SSBs (under stack pressure) may potentially lead to changes in the SEI composition. Since our results show the presence of several phases, the local distribution of elements is analyzed using EDX mapping.

The expanded SEM image of a single large bulk-SEI particle, along with EDX mapping for sulfur, phosphorous, and chlorine, is shown in Figure 4. It reveals a predominant sulfur signal, which may indicate the distribution of Li_2S. Considering the non-uniformity in the predominant sulfur signal and by reviewing the combined mapping, domains with distinct phases are found. This becomes obvious in regions

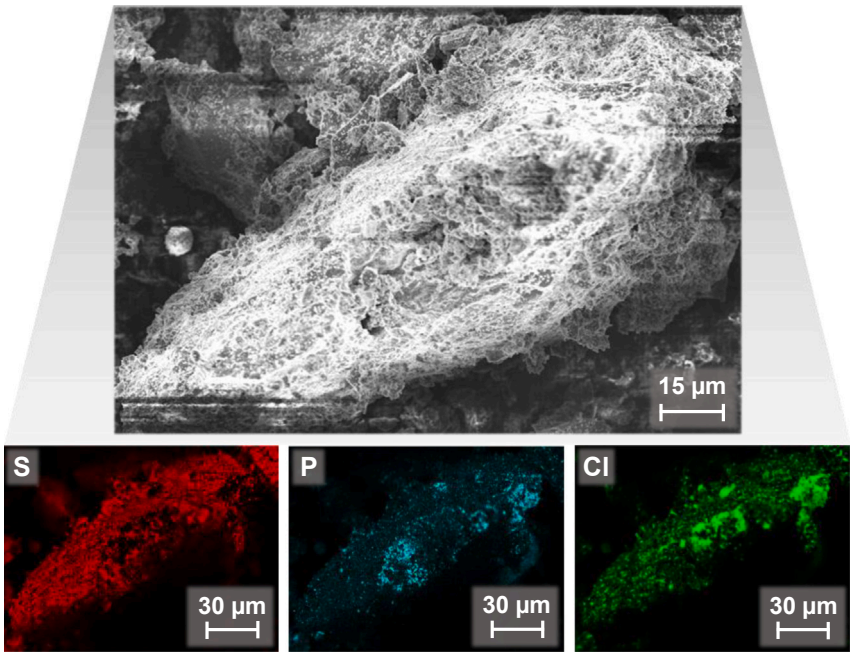

Figure 4. SEM image and corresponding EDX element mappings of one bulk-SEI particle
SEM image (top) and EDX element mappings (bottom) were recorded at 8 kV for the elements sulfur, phosphorous, and chloride. Areas with elevated concentrations of sulfur, phosphorous, and chlorine are found, represented by the corresponding $K_{\alpha 1}$ lines, which likely indicate the distribution of Li_2S, Li_3P, and LiCl, respectively.

where the sulfur signal is weak, and elevated concentrations of phosphorus and chlorine are detected. The latter signals may indicate the presence and distribution of Li_3P (or other phosphorous species) and LiCl, respectively. Below, we will discuss the potential domain structure and the effect of non-uniform distribution of individual phases in multiphase SEIs.

Upon reviewing the elemental quantification for these three elements, we note mass ratios of 66 wt % for sulfur, 15 wt % for phosphorous, and 19 wt % for chlorine. The deviations, especially in the chlorine signal, can be attributed to the LiCl impurity phase in the starting LPSCl material, as identified by XRD refinement (refer to Figure S5). Reference measurements of pristine LPSCl determined a mass ratio of 68 wt % for sulfur, 14 wt % for phosphorous, and 18 wt % for chlorine (Figure S16; Section G, supplemental information). Hence, the obtained quantification of the bulk-SEI shows only minor shifts in the elemental ratio after synthesis. While the mass ratio of sulfur decreased, the elemental concentrations of phosphorus and chlorine increased slightly as well. However, this variation falls within the accuracy of EDX measurements. At this point, we want to emphasize that these EDX results solely reveal the elemental fractions, regardless of their binding state and chemical environment.

Assuming for simplicity that sulfur, phosphorous, and chlorine are mainly bound in SEI species, the mass ratios match well with the theoretical values of 71 wt % Li_2S, 16 wt % Li_3P, and 13 wt % LiCl for the SEI. For the sake of completeness, the elemental distribution of oxygen (in total, 5 wt %) is shown in Figure S17 (Section G, supplemental information). Signals of oxygen are evenly distributed across the particle surface at comparable low concentration. We assume that

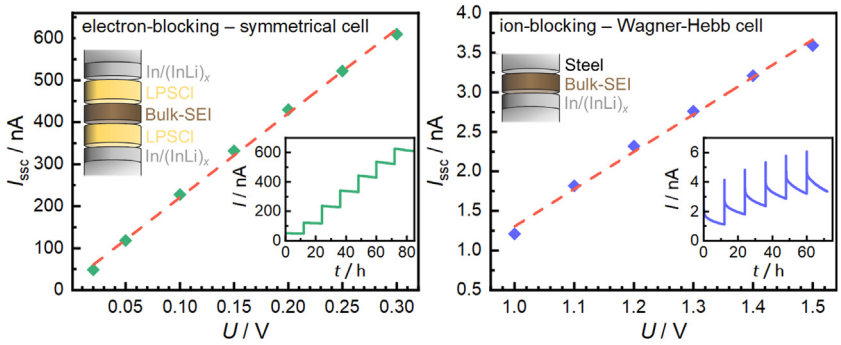

Figure 5. Determination of partial conductivities by dc polarization using selectively blocking cell configurations

(A and B) The electron-blocking setup and respective I_{ssc}-V correlation (A) and the ion-blocking Wagner-Hebb setup and respective I_{ssc}-V correlation (B) are used to evaluate σ_{ion} and σ_{el}, respectively. This is done by linearly fitting the data (red dashed lines) and using Equation 2. Each steady-state current I_{ssc} is obtained by analyzing the initial I-V curves (inlays) at different applied voltages for 12 h (at each voltage).

(surface) contaminations, e.g., lithium hydroxide as identified by XPS, are the reason for the observed oxygen signals due to reactions with trace amounts of oxygen and moisture. However, this is not necessarily indicating or evidencing the presence (or position) of residual lithium metal precursors since naturally formed SEI can also consist of species containing oxygen.

Conduction properties

The conduction characteristics ultimately determine the nature and growth of SEIs. Therefore, a comprehensive investigation and quantification of both the partial ionic (σ_{ion}) and electronic conductivity (σ_{el}) of SEIs play pivotal roles in assessing SEI growth and its long-term impact on battery performance.

We expect the SEI to be a mixed ion-electron conductor with low partial conductivities. Hence, conductivity measurements on pure bulk-SEI powder were performed to investigate its partial ionic and electronic transport properties. Moreover, the observed conductivity may also indicate the presence of residual precursor material, as remains of lithium metal and LPSCl should increase σ_{el} and σ_{ion}, respectively. Since impedance measurements were found to be ineffective in deconvoluting the partial conductivities, we used dc polarization. Specifically, dc Wagner-Hebb measurements with one selectively blocking electrode are reported to effectively separate (low) ionic and electronic conductivities at fixed redox potentials (i.e., controlled lithium-ion activities).[43,44]

Unfortunately, for assessing σ_{ion}, the corresponding Wagner-Hebb configuration (with one electron-blocking and one reversible electrode) was unsuitable due to the lack of stable conditions. Thus, two electron-blocking electrodes were utilized (depicted in Figure 5A). σ_{ion} is calculated by taking the slope from linear regression for the steady-state current I_{ssc} of successive dc measurements under electron-blocking conditions (see Figure 5A) according to Equation 2:

$$\sigma_i = \frac{dI_{res}}{dV} \cdot \frac{l}{A} \qquad \text{(Equation 2)}$$

with V being the applied voltage, l the pellet thickness, A the cell area, and i indicating the respective charge carrier—for either ionic (ion) or electronic (el) conduction.

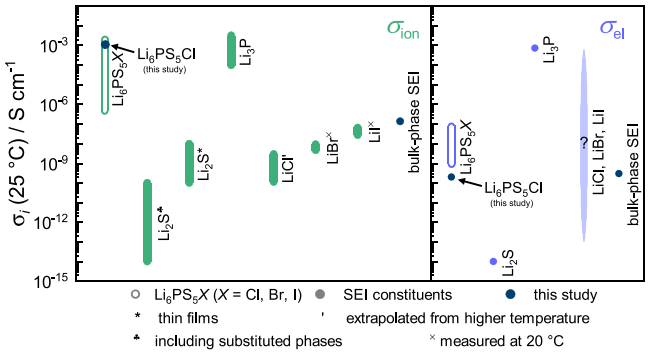

Figure 6. The partial ionic and electronic conductivities σ_i (i = ion and el, respectively) at 25°C of Li_6PS_5X (X = Cl, Br, and I; excluding substituted phases) and their typical SEI constituents

σ_i of the bulk-SEI and the initially used sulfide SE (Li_6PS_5Cl) in this work are depicted in dark blue. For some materials, a range of values is reported by different authors. The values of Li_6PS_5X (X = Cl, Br, and I),[53–58] Li_2S,[59–61] Li_3P,[62–64] LiCl,[65,66] LiBr,[66,67] and LiI[66–69] were taken from the reported data. An asterisk, an apostrophe, a spade, and a cross indicate the values for thin film materials, data estimated by extrapolation from higher temperatures, data including substituted phases, and data recorded at 20°C, respectively.

We determined the room temperature (25°C) partial ionic conductivity to be σ_{ion} = 134 nS cm^{-1} for the bulk-SEI of LPSCl. To put this value within a wider context, we further compare reported conductivity values for various single-phase SEI constituents of lithium argyrodites Li_6PS_5X (X = Cl, Br, I) (Figure 6, left). It is noteworthy that neither the individual values for these SEI constituents (i.e., Li_2S, Li_3P, and LiCl) nor the value of the LPSCl used align with σ_{ion} estimated in this study (represented in dark blue, σ_{ion} = 134 nS/cm). This proves a substantial underestimation of the SEI's partial ionic conductivity compared with several previous studies (related to various sulfide SEs) by at least one order of magnitude when simply assuming the ionic conductivity of bulk-type, microcrystalline Li_2S.[46] As will be shown below, this underestimation results in inaccurate approximations of the SEI layer thickness (and potentially other properties). Nevertheless, this discrepancy is particularly relevant given that Li_2S constitutes the dominant volume fraction within the SEI, accounting for 71 vol %. Consequently, other SEI constituents (i.e., Li_3P) must enable a higher overall ionic conductivity, or the Li_2S formed in the (bulk-)SEI has a higher conductivity than bulk-Li_2S, e.g., due to amorphous phase fractions, nanocrystalline regions, or interface contributions. A more thorough examination of this observation, however, falls outside the scope of this study and requires further investigation. Please note once more that the heat treatment during synthesis may lead to deviations from the actual SEI at the Li|LPSCl interface, potentially affecting both the formation of phases and the overall conductivity. It is our working hypothesis that we come close to the true SEI with our approach, as confirmed below by the quantitative SEI growth considerations.

σ_{el} was determined by dc Wagner-Hebb measurements with one ion-blocking and one reversible electrode (depicted in Figure 5B) and calculated (using Equation 2) to be σ_{el} = 0.3 nS cm^{-1} at room temperature for the bulk-SEI of LPSCl. In Figure 6 (right), this value is compared with reported conductivity values for some single-phase SEI constituents of lithium argyrodites Li_6PS_5X (X = Cl, Br, I). While it agrees well with the value of the LPSCl used, it may not indicate an increased dendrite risk with respect to its comparable σ_{el}. Further, it clearly deviates from the reported electronic conductivity of bulk-Li_2S (~0.1 pS cm^{-1}) by a factor of three orders of magnitude.[61] This latter value is commonly used for the approximation of the conduction

properties of SEIs. The origin of this value for Li_2S remains unspecified by the authors. Comparing the value for (crystalline) Li_3P, it appears again that each SEI constituent may contribute to the overall σ_{el} of the bulk-SEI. Please note that the values for σ_{ion} and σ_{el} of crystalline Li_3P serve as a preliminary approximation, although they may differ from those in the amorphous state or in other Li_xP compounds. Unfortunately, to the best of our knowledge, reliable values for σ_{el}, especially for LiCl but also for LiBr and LiI, have not been reported in literature. Thus, we like to emphasize that the lack of reliable information on σ_{el} of corresponding binary lithium compounds hinders further analysis and calls for additional experimental studies.

These measurements and results represent the first experimental data being reported for the σ_{ion} and σ_{el} of SEI-type materials. The values obtained in this study can serve as valuable parameters for assessing further SEI properties by simulation and modeling.

SEI growth kinetics and implications for SSBs

Consequently, we intend to assess the partial conductivities of ionic and electronic charge carriers in the SEI with regard to their implication on SSB performance and lifetime. When comparing the ionic conductivity of lithium argyrodites Li_6PS_5X (X = Cl, Br, I) (shown left in Figure 6), it becomes evident that the SEI conductivity exhibits a significantly lower conductivity than the lithium argyrodites. Notably, the difference becomes especially pronounced (several orders of magnitude) when compared with lithium argyrodites with high ionic conductivity (as utilized in this study, represented in dark blue).

In order to compute various properties and assess potential implications, we consider published data for SEI resistances extracted from impedance measurements. Riegger et al.[27] documented area-specific ionic resistances of up to 80 Ω cm^2 for multiphase SEI layers of degraded LPSCl (in contact to passivated lithium foil). Using this value, as well as σ_{ion} from our study, and assuming self-limited growth, we estimate a SEI layer thickness of up to d $\sim$ 110 nm. This thickness estimation is plausible, considering that the partial ionic conductivity within nanoscale multiphase layers may locally increase. Consequently, this would mark a further increase in SEI layer thickness.

Wenzel et al.[46] estimated a SEI layer thickness of only a few nm by the analysis of impedance measurements. However, the authors based their assumptions on the SEI's partial ionic conductivity on the properties of bulk-Li_2S, which substantially underestimates the SEI's partial ionic conductivity, as discussed above. Thus, the estimates of SEI layer thickness by Wenzel et al. are too low by at least one order of magnitude.

However, for a comprehensive analysis of SEI growth, it is essential to take kinetic considerations into account. The diffusion-controlled growth of the SEI can be approximated and described by a Wagner-type diffusion model if the growing layer is approximated as a dense and fully covering interphase. Adapting this model leads to Equation 3, with a square-root of time behavior for the consumption of SE material:[19]

$$d = \sqrt{\frac{2}{F^2 \cdot \rho_{SEI} \cdot x} \frac{M_{SEI} \cdot \sigma_{el} \cdot \sigma_{ion}}{\sigma_{el}+\sigma_{ion}} \cdot \mu_{Li}^0 \cdot \sqrt{t}} \cong \sqrt{\frac{2}{F^2 \cdot \rho_{SEI} \cdot x} M_{SEI} \cdot \sigma_{el} \cdot \mu_{Li}^0 \cdot \sqrt{t}} = k \cdot \sqrt{t} \quad \text{(Equation 3)}$$

with d, F, ρ_{SEI}, x, M_{SEI}, σ_{ion}, σ_{el}, μ^0_{Li}, t, and k being the SEI layer thickness, the Faraday constant, the mean density of the SEI, the stoichiometric factor (moles of the lithium metal required for the stoichiometric decomposition reaction—in our case 8), the mean molar mass of the SEI, the mean ionic and electronic conductivity of the SEI, the chemical potential of pure lithium metal (μ^0_{Li} = 8.35 kJ mol^{-1}), the reaction time, and the parabolic rate constant, respectively. This equation was derived by approximating the gradient of the chemical potential by μ^0_{Li}/d, as described elsewhere.[26] Additionally, it is important to highlight that Equation 3 is applicable under conditions of one-dimensional transport, purely chemical potential gradient-driven flux, and boundaries with constant chemical potentials.[70]

Further, Equation 3 can be transferred to Equation 4 by substituting d with $\sigma_{SEI} = d/R_{SEI}$ and assuming $\sigma_{SEI} \cong \sigma_{ion} \gg \sigma_{el}$, with σ_{SEI} being the mean SEI conductivity and R_{SEI} being the area-specific ionic resistance of the SEI:

$$R_{SEI} = \frac{1}{\sigma_{SEI}} \cdot \sqrt{\frac{2}{F^2 \cdot \rho_{SEI} \cdot x} \frac{M_{SEI} \cdot \sigma_{el} \cdot \sigma_{ion}}{\sigma_{el}+\sigma_{ion}} \cdot \mu^0_{Li}} \cdot \sqrt{t} \cong \frac{1}{\sigma_{ion}} \cdot \sqrt{\frac{2}{F^2 \cdot \rho_{SEI} \cdot x} M_{SEI} \cdot \sigma_{el} \cdot \mu^0_{Li}} \cdot \sqrt{t} = k' \cdot \sqrt{t} \quad \text{(Equation 4)}$$

Hence, a new parabolic rate constant k' is derived, describing the temporal evolution of resistance due to SEI growth. Consequently, the SEI growth can be anticipated to extrapolate the SEI layer thickness and the corresponding SEI resistance over extended periods (i.e., up to the typical battery lifetime of 10 years). Taking Equations 3 and 4 as well as the findings from our study on σ_{ion} and σ_{el} of the bulk-SEI, the parabolic rate constants were calculated to be k = 0.43 nm s$^{-0.5}$ and k' = 320 mΩ cm^2 s$^{-0.5}$ for LPSCl. After 1 day, the SEI layer thickness is approximated to be d = 126 nm with a resistance of R_{SEI} = 95 Ω cm^2. These values increase from 334 nm and 250 Ω cm^2 to 7.6 μm and 5.7 kΩ cm^2 over a period of 1 week and 10 years, respectively. This agrees well with recent findings on SEI layer thickness by Aktekin et al.[28] and Otto et al.[29] of ~315 and ~305 nm for 1 week (from electrochemical titration and ToF-SIMS studies), respectively. Therefore, the values obtained for σ_{ion} and σ_{el} in this study validate previous findings on the SEI dimensions.

The very good agreement between our current results and the SEI growth kinetics determined using a completely different electrochemical approach (i.e., coulometric titration time analysis, CTTA, in anode-free cells) demonstrates the viability of our bulk-SEI synthesis approach. Figure S18 (Section H, supplemental information) compares the temporal evolution of SEI growth predicted from bulk-SEI properties using the Wagner-type diffusion model (d_{SEI} vs. t or $t^{0.5}$) with the SEI growth quantitatively observed in CTTA experiments.[28] In this comparison, Equation 3 and the parabolic rate constant (k = 0.43 nm s$^{-0.5}$) obtained in our study were used. Conversely, CTTA results can also be used to calculate k and σ_{el} from the slope of the linear fit in d_{SEI} vs. $t^{0.5}$ and Equation 3, yielding values of 0.46 nm s$^{-0.5}$ and 0.34 nS cm^{-1}, respectively. These numbers closely match the values determined for the bulk-SEI in this study (k = 0.43 nm s$^{-0.5}$ and σ_{el} = 0.3 nS cm^{-1}). This agreement with the naturally formed SEI in a real cell, along with the characterization results of the synthesized bulk-SEI, provides strong evidence for: (1) a minimal to negligible impact of the elevated reaction temperature used; (2) unaltered bulk-SEI properties by potentially present precursor material traces (in respect to various properties)—or that the cell-level SEI also contains the same unreacted or unknown minor phases; (3) an effective simulation of multiphase SEI properties via bulk-SEI synthesis; and (4) an accurate modeling of transport parameters derived from those properties to predict SEI

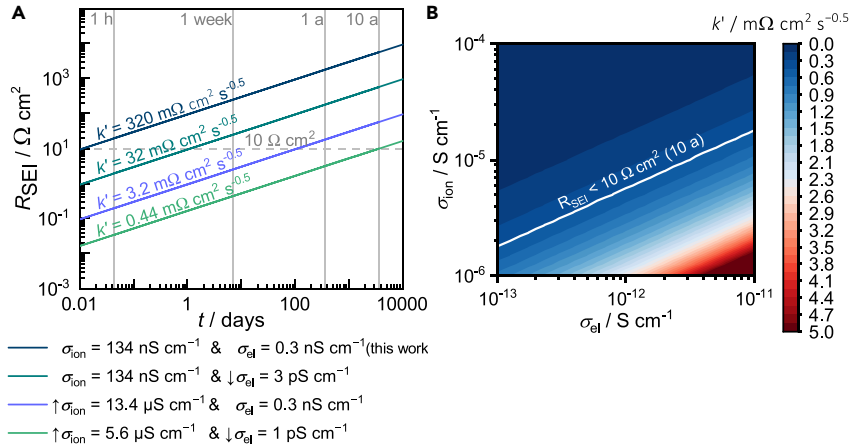

Figure 7. Modeling of the SEI (ionic) resistance as a function of time and the parabolic rate constant k' as a function of σ_{ion} and σ_{el}

(A) The SEI (ionic) resistance is calculated as a function of time for different combinations of σ_{ion} and σ_{el}, including the results of this work. The corresponding k' values are denoted on each profile. As a demonstration, we varied both partial conductivities by 2 orders of magnitude. A potential threshold for an optimized SEI resistance at 10 Ω cm^2 is marked (in gray), requiring k' to be less than 0.44 mΩ cm^2 s$^{-0.5}$ for a lifetime of 10 years (indicated in green).

(B)The contour map of the parabolic rate constant k' is calculated for values up to 5 mΩ cm^2 s$^{-0.5}$. The threshold value of 0.44 mΩ cm^2 s$^{-0.5}$ indicates a SEI (ionic) resistance of ~10 Ω cm^2 and lower over a period of 10 years.

growth and kinetics in SSB cells. Additionally, the combination of both approaches validates the application of the Wagner-type diffusion model for the detailed analysis and description of SEI growth.

Hence, the good agreement between two entirely different approaches is a significant validation for the effectiveness of our synthetic SEI approach. Our experimental results on the partial conductivities enable kinetic considerations and calculations in estimating SEI growth using Wagner-type diffusion models. Consequently, we anticipate that our data will establish crucial parameters and encourage further endeavors in future simulations and modulations of SEI growth. In particular, we want to emphasize that our findings can serve as the basis for designing SEs that combine both high ionic conductivity and stable yet minimized SEI formation. This is discussed in the next section.

Randau et al.[1] emphasized that the cell impedance of operational SSBs should not exceed a value of 40 Ω cm^2 but rather should be even lower to meet the typical resistances of LIBs. As a potential threshold for SEI resistance, we consider 10 Ω cm^2 to be a reasonable value to ensure the sufficient kinetic performance of SSBs. Therefore, we calculated the resistance increase of the SEI for up to 10 years (according to Equation 4) for different partial conductivities (σ_{ion} and σ_{el}) and resulting k' values (see Figure 7A).

Starting from the partial conductivities obtained in this study, it is demonstrated that reducing σ_{el} and increasing σ_{ion} leads to a decrease in the parabolic rate constant and, consequently, a decrease in resistance (and thickness) over time. Combining both reduces k' further (as seen in the green line). While a value of 32 mΩ cm^2 s$^{-0.5}$ for k' is insufficient to significantly reduce the SEI resistance, a reduction to less than 5 mΩ cm^2 s$^{-0.5}$ seems suitable for several weeks to months. However, to meet the long-term criteria of 10 Ω cm^2 over 10 years, further reduction

of k' to ~0.44 mΩ cm^2 s$^{-0.5}$ is crucial—or finding a mechanism to stop the diffusion-controlled SEI formation at all. To complete the picture: with an upper limit of 0.44 mΩ cm^2 s$^{-0.5}$ for k', this corresponds to a growth rate of $k \leq 0.25$ pm s$^{-0.5}$ and a SEI layer thickness of $d \leq 4.4$ nm after 10 years.

Hence, our experimental findings and computations underscore the need for SEI optimization to decrease its impedance and growth rate to stabilize the Li|SE interface (i.e., by reducing the mean σ_{el} or improving the mean σ_{ion} of SEIs). However, suitable values for k' can be achieved through various combinations of σ_{ion} and σ_{el}. Therefore, we plotted the relationship between k' and σ_{ion} as well as σ_{el}, considering values up to 5 mΩ cm^2 s$^{-0.5}$ in Figure 7B. The findings from Figure 7A served as a threshold value ($k' < 0.44$ mΩ cm^2 s$^{-0.5}$, white profile).

In line with Equation 4, k' exhibits a reciprocal relationship with σ_{ion}, whereas it follows a square-root relationship with σ_{el}: $R_{SEI} \sim \sigma_{ion}^{-1} \cdot \sigma_{el}^{0.5}$. Therefore, enhancing σ_{ion} is a more effective strategy for optimizing the Li|SE interface. However, considering feasibility, we assume that improving σ_{ion} of the SEI up to 10^{-4} S cm^{-1} is unlikely, given the typical values for σ_{ion} in common SEs (~10^{-3} S cm^{-1}). As a result, it becomes crucial to optimize both σ_{ion} and σ_{el} of the SEI to facilitate the long-term viability of SSBs for practical applications. We like to highlight the critical role of Li_3P for the SEI growth and resistance, as it appears to be a true mixed conductor. Its volume fraction is below the typical limit for 3D percolation, but it will increase the mean ionic conductivity of the SEI and thus reduce R_{SEI}. Unfortunately, it will also increase the mean electronic conductivity of the SEI and thus increase the growth rate of the SEI. It is worth noting that Na_3P is the critical SEI component in the analog case of SEI formation in sodium thiophosphates like Na_3PS_4. As demonstrated by Wenzel et al.,[71] Na_3PS_4 degrades rapidly by reaction with sodium metal, as the volume fraction of Na_3P in the SEI is even higher than in the case of Li_6PS_5Cl, and as Na_3P has a higher electronic conductivity than Li_3P.

The question whether SEI layers in SSBs exhibit self-limiting growth remains controversial, given that the growth rate (i.e., k) of the SEI is determined by σ_{el} (with respect to Equation 3: $R_{SEI} \sim \sigma_{el}^{0.5}$). The value of σ_{el} determined in this study cannot be disregarded and raises doubts about the self-limited growth mode during SEI evolution. In a recent theoretical study on $Li_xPO_yN_z$, Li et al.[72] emphasized the critical importance of low electronic conductivity in preventing SEI formation, achieving interface stabilization.[38] This would consequently lead to a thin SEI layer and minimal interphase resistance. Please note that $Li_xPO_yN_z$ shows the lowest reported values for σ_{el} in literature for a SE (10^{-14}–10^{-12} S cm^{-1}).[73–75] Our findings strongly suggest that σ_{el} of the multiphase SEI investigated in our study will be too high to effectively impede ongoing SEI growth in lithium thiophosphate-based SSBs, as long as no reasonable countermeasure is being taken. However, it is important to note that the electronic insulating properties of multiphase SEIs are not thoroughly explored or comprehensively understood yet, making additional assessments speculative. We also need to stress that our knowledge on the role of the SEI in thiophosphate electrolytes is limited. Cells in academic labs will usually not be studied longer than a few weeks. The resistance growth due to SEI formation may not be critical within the period of time, and thus, is probably underrated.

Upon assessing the potential consequences for SSBs by the multiphase SEI's conduction properties evaluated here, further aspects require consideration. The separation of individual phases within the multiphase bulk-SEI observed in EDX measurements may suggest the presence of advantageous conduction pathways on the

nanoscale, potentially leading to percolation phenomena along interfaces. Independent on the actual microstructure (i.e., domains or layers), advantageous conduction pathways within SEI layers may have detrimental effects on the long-term performance of SSBs. On the one hand, beneficial ionic pathways (i.e., by Li_3P) may support the conduction of lithium ions, effectively bypassing regions with lower ionic conductivity (i.e., Li_2S and LiCl). Resulting in inhomogeneous Li|SEI|SE interface conditions, this would hinder a homogeneously distributed lithium-ion flux during battery cycling due to increased constriction phenomena,[76] and disturb the formation of uniform metal stripping and plating morphologies. On the other hand, the existence of favorable electronic pathways by individual phases will strongly influence the SEI growth, leading to inhomogeneous and ongoing SEI formation, eventually causing cell failure. Hence, our EDX studies underscore the essential need for comprehensive investigations into the microstructure of composite (multiphase) SEI layers in future research.

We like to emphasize the importance of implementing effective measures—during the design of SEs—to stabilize and suppress interphase evolution for the above consequences. The inherent characteristics of multiphase SEI layers require optimization, especially with regard to σ_{ion} and σ_{el}, to effectively minimize implications for SSBs. The ionic impedance and layer thickness of SEIs currently prevent the development of long-term operational SSBs with lithium metal, once unmodified sulfide SEs are used. Hence, controlling the interface and interphase properties can ultimately lead to the realization of SSBs through the integration of LMAs, positioning SSBs as viable competitors to LIBs. One possible approach involves examining and enhancing fully reduced SEs that are thermodynamically stable at low operating potentials, aiming to eliminate degradation.[77,78] If (inorganic) modifications of sulfide SEs are found to be inadequate, introducing artificial interlayers (e.g., polymer-based ones) with moderate to high ionic conductivity and electronic insulating characteristics could potentially facilitate the stabilization of the Li|SE interface. We would like to note that Guo et al.[30] provide a more in-depth discussion of challenges of various engineering approaches at the Li|SE interface.

Conclusions

In this study, we present a novel and well transferable approach to simulate the degradation of various sulfide SEs, aiming to gain a deeper understanding of the properties of multiphase SEIs. Through a bulk-type solid-state reaction between the SE and micron-sized lithium particles, we obtain a composite of binary lithium phases that we suggest as a reasonable model for the SEI in SSB cells with LMAs. The formation of a bulk-SEI comprising Li_2S, Li_3P, and LiCl from the model electrolyte Li_6PS_5Cl and lithium metal powder has been proven. Subsequent conductivity measurements resulted in both partial ionic and electronic conductivity directly from the bulk-SEI material. The results reveal a significant underestimation in prior reports, particularly in case of the ionic conductivity by at least one order of magnitude. On the one hand, the electronic conductivity of the SEI controls its temporal evolution and its thickness as function of time. On the other hand, the ionic conductivity governs the resistance of the SEI, influencing both the performance and lifetime of SSBs. We hope that our experimental data (i.e., σ_{ion} and σ_{el}) will establish crucial benchmark parameters for upcoming simulations and further experimental evaluations. Our findings and computational results underscore the need to optimize the Li|SE interface and both partial conductivities, while motivating for further exploration and innovation to achieve lithium thiophosphate-based SSBs with high energy and power density.

EXPERIMENTAL PROCEDURES

Resource availability

Lead contact

Further information and requests for resources and reagents should be directed to and will be fulfilled by the lead contact, Jürgen Janek (juergen.janek@pc.jlug.de).

Materials availability

This study did not generate new, unique reagents.

Data and code availability

All data associated with the study are included as supplemental data with this article.

Synthesis and cell assembly were carried out in an argon-filled glovebox (*LabMaster-PRO*, MBraun, Garching, Germany), with $p(O_2)/p$ and $p(H_2O)/p < 1$ ppm. Electrochemical measurements were carried out in sealed cell casings at 25°C using a *VMP 300* potentiostat (BioLogic, Seyssinet-Pariset, France).

Preparation of materials

The lithium metal powder utilized in this study was synthesized by (droplet) emulsion, similar to the method described in elsewhere.[79] To this end, tetradecane (anhydrous, 99+ %, Sigma-Aldrich, Germany) as inert medium was gradually heated to 270°C in a custom-built stainless-steel reactor using a hotplate. The temperature was then maintained for 5 min to ensure thermal equilibration. Subsequently, 0.7–1 g of small lithium chunks, obtained by cutting lithium metal rods (99.8%, abcr, Germany), were added to the reactor. To achieve complete melting of lithium metal, the reactor was heated for additional 10 min. To create a lithium metal droplet emulsion, the tetradecane and lithium melt were stirred at 26,000 rpm for 5 min using an *X10* stirrer equipped with a *10G* tool (ystral, Germany). Once the stirring stopped, the mixture was slowly cooled down to ambient temperature, causing the lithium droplets to solidify into lithium metal particles. Subsequently, the inert liquid was removed via filtration, and the lithium metal powder was rinsed three times with hexane (anhydrous, 95%, Sigma-Aldrich, Germany). Lastly, the powder was dried at room temperature under argon to eliminate any remaining traces of tetradecane and hexane.

To synthesize bulk material (bulk-SEI) corresponding to the composition of the SEI, lithium argyrodite Li_6PS_5Cl (LPSCl) as SE (POSCO JK Solid Solution, Yangsan, South Korea) was mixed with a stochiometric amount of freshly prepared lithium metal powder based on the chemical reaction (Equation 1). Through grinding by hand in an agate mortar, a homogeneous mixture was achieved after 10 min, accompanied by a noticeable darkening of color. The mixture was then subjected to heating at 250°C for several hours under dynamic vacuum in an *MB-VOH-600* oven (MBraun, Garching, Germany). This additional heat treatment is used to complete the reaction between reactants. The resulting powder exhibited a reddish-brown color and was once more hand-ground to achieve a finer texture.

The morphology of the synthesized bulk-SEI was investigated by means of SEM using a field emission *GeminiSEM 560* (Carl Zeiss Microscopy, Oberkochen, Germany). For sample transfer, a transfer module system *EM VCT500* (Leica, Wetzlar, Germany) was used to prevent the exposure of samples to moisture and atmosphere. SEM images were taken using a secondary electron detector. Complementary EDX was performed using a *ULTIM MAX* EDX detector with 170 mm^2 SSD sensor (Oxford Instruments NanoAnalysis, High Wycombe, UK). The electron acceleration voltage during

spectra acquisition was set to 8 kV, images are acquired with a resolution of 512 pixels (100 μs pixel dwell time). Measurements of several different particles were conducted. The software *AZtec 4.3* (Oxford Instruments NanoAnalysis, High Wycombe, UK) was used for automatic identification and quantification of the elements sulfur, phosphorous, chlorine, and oxygen.

Characterization

XRD and XPS were employed for structural and detailed chemical analysis, respectively. The powder XRD pattern was obtained using an *Empyrean 2* diffractometer (Malvern Panalytical Ltd, Malvern, UK) configured in θ-θ geometry and equipped with a sample spinner. A monochromatic Cu-K_α X-ray beam with a wavelength of 154 pm was used. The measurements were conducted at an operating voltage of 40 kV and 40 mA, with a step size of 0.026° and a duration of 200 s per step. To prevent contamination during measurement, a polyimide foil was used to seal the sample under argon atmosphere. Rietveld refinements were carried out utilizing *TOPAS Academic v6.0* software[80] in combination with coding program jEdit.[81]

XPS measurements were conducted with a *Versaprobe 4* (ULVAC-PHI, Inc., Chanhassen, USA). A monochromatized Al K_α X-ray source was employed (beam diameter of 200 μm, X-ray power of 50 W), while the pressure in the XPS chamber was in the range of 10^{-7} to 10^{-6} Pa and the sample surface was charge neutralized by slow electrons and argon ions during measurements. XPS depth profiling was performed by Ar^+ sputtering with a grid size of 2 × 2 mm^2 with an initial sputtering step of 0.5 kV for 1 min, followed by a step of 1 kV for 1 min, and five sputtering steps of 2 kV for 1 min each. Using a transfer shuttle, cross contaminations with atmosphere were avoided. Data analysis was carried out with the *CasaXPS* software (Casa Software, Devon, UK).

Cell assembly and electrochemical testing

For measurements of the partial ionic conductivity, an electron-blocking symmetric cell configuration was used. 80 mg of bulk-SEI were compacted by hand in a polyether-ether-ketone casing using stainless-steel pistons. 80 mg of sulfide SE (LPSCl) were homogeneously distributed on each side of the bulk-SEI. By applying a uniaxial pressure of 380 MPa for 3 min at room temperature, the layered materials were densified, resulting in a pellet thickness of ∼520 μm for the bulk-SEI. Finally, indium foil (100 μm thickness, 9 mm diameter, 99.999%, ChemPUR, Germany) and lithium foil (100 μm thickness, 6 mm diameter, 99.9%, China Energy Lithium, China) were placed on both sides of the stack to serve as lithium reservoir. Lithium diffuses into the indium metal and forms an $In/(InLi)_x$ phase field with a stable potential of 0.62 V vs. Li^+/Li.[82]

For the measurement of the partial electronic conductivity using Wagner-Hebb dc polarization,[43,44] a one-sided ion-blocking cell configuration was utilized. 80 mg of bulk-SEI were directly compressed at 380 MPa for 3 min at room temperature. While one side of the pellet was equipped with a reversible $In/(InLi)_x$ electrode, the employed stainless-steel piston served as an ion-blocking electrode on the other side. The ion-blocking electrode (steel) and the reversible electrode ($In/(InLi)_x$) served as working electrode and counter electrode, respectively.

Consecutively, while applying a pressure of 40 MPa to the cell stack, the different partial charge carrier conductivities were evaluated through dc polarization at different applied potentials. The potential range was 20–300 mV and 1.0–1.5 V for the electron- and ion-blocking cell, respectively. The current response was continuously monitored for 12 h at each potential step to determine the respective conductivity from the steady-state current I_{ssc}. After a waiting period of at least 6 h, we

consider the system to be in a steady state if the current response has remained stable within 3% over 1 h (or longer).

SUPPLEMENTAL INFORMATION

Supplemental information can be found online at https://doi.org/10.1016/j.joule.2024.07.006.

ACKNOWLEDGMENTS

The authors thank Dr. Felix Hartmann for his help with the Rietveld refinement of X-ray diffractograms. We thank Dr. Christian Schneider and Dr. Max Plass for their help in synthesizing Li_3P reference material. C.D.A. and J.J. acknowledge the financial support by the Bundesministerium für Bildung und Forschung (BMBF) within the ALANO project (grant no. 03XP0396J). P.M., L.M.R., B.A., and J.J. acknowledge funding by the BMBF within the FestBatt—Cluster of Competence for Solid-State Batteries (grant nos. 03XP0433D and 03XP0430A).

AUTHOR CONTRIBUTIONS

C.D.A.: conceptualization, methodology, validation, formal analysis, investigation, writing—original draft, writing—review & editing, visualization; N.U.C.B.M.: investigation; L.M.R.: investigation; B.A.: investigation, formal analysis, writing—review & editing; P.M.: conceptualization, methodology, investigation; K.P.: investigation, project administration, funding acquisition; J.J.: conceptualization, methodology, resources, supervision, writing—original draft, writing—review & editing, and funding acquisition.

DECLARATION OF INTERESTS

The authors declare no competing interests.

DECLARATION OF GENERATIVE AI AND AI-ASSISTED TECHNOLOGIES IN THE WRITING PROCESS

During the preparation of this work, the authors used *ChatGPT 3.5* (by OpenAI) to improve readability and language. After using this tool, the authors reviewed and edited the content as needed and take full responsibility for the content of the publication.

Received: March 1, 2024
Revised: April 22, 2024
Accepted: July 12, 2024
Published: August 12, 2024

REFERENCES

1. Randau, S., Weber, D.A., Kötz, O., Koerver, R., Braun, P., Weber, A., Ivers-Tiffée, E., Adermann, T., Kulisch, J., Zeier, W.G., et al. (2020). Benchmarking the Performance of All-Solid-State Li Batteries. Nat. Energy *5*, 259–270. https://doi.org/10.1038/s41560-020-0565-1.

2. Liu, J., Bao, Z., Cui, Y., Dufek, E.J., Goodenough, J.B., Khalifah, P., Li, Q., Liaw, B.Y., Liu, P., Manthiram, A., et al. (2019). Pathways for Practical High-Energy Long-Cycling Li-Metal Batteries. Nat. Energy *4*, 180–186. https://doi.org/10.1038/s41560-019-0338-x.

3. Bachman, J.C., Muy, S., Grimaud, A., Chang, H.-H., Pour, N., Lux, S.F., Paschos, O., Maglia, F., Lupart, S., Lamp, P., et al. (2016). Inorganic Solid-State Electrolytes for Lithium Batteries: Mechanisms and Properties Governing Ion Conduction. Chem. Rev. *116*, 140–162. https://doi.org/10.1021/acs.chemrev.5b00563.

4. Wang, M.J., Kazyak, E., Dasgupta, N.P., and Sakamoto, J. (2021). Transitioning Solid-State Batteries from Lab to Market: Linking Electro-Chemo-Mechanics with Practical Considerations. Joule *5*, 1371–1390. https://doi.org/10.1016/j.joule.2021.04.001.

5. Famprikis, T., Canepa, P., Dawson, J.A., Islam, M.S., and Masquelier, C. (2019). Fundamentals of Inorganic Solid-State Electrolytes for Batteries. Nat. Mater. *18*, 1278–1291. https://doi.org/10.1038/s41563-019-0431-3.

6. Bates, A.M., Preger, Y., Torres-Castro, L., Harrison, K.L., Harris, S.J., and Hewson, J. (2022). Are Solid-State Batteries Safer than Lithium-Ion Batteries? Joule *6*, 742–755. https://doi.org/10.1016/j.joule.2022.02.007.

7. Kato, Y., Hori, S., Saito, T., Suzuki, K., Hirayama, M., Mitsui, A., Yonemura, M., Iba, H., and Kanno, R. (2016). High-Power All-Solid-State

Batteries using Sulfide Superionic Conductors. Nat. Energy *1*, 16030. https://doi.org/10.1038/nenergy.2016.30.

8. Patel, S.V., Banerjee, S., Liu, H., Wang, P., Chien, P.-H., Feng, X., Liu, J., Ong, S.P., and Hu, Y.-Y. (2021). Tunable Lithium-Ion Transport in Mixed-Halide Argyrodites $Li_{6-x}PS_{5-x}ClBr_x$: An Unusual Compositional Space. Chem. Mater. *33*, 1435–1443. https://doi.org/10.1021/acs.chemmater.0c04650.

9. Janek, J., and Zeier, W.G. (2016). A Solid Future for Battery Development. Nat. Energy *1*, 16141. https://doi.org/10.1038/nenergy.2016.141.

10. Krauskopf, T., Richter, F.H., Zeier, W.G., and Janek, J. (2020). Physicochemical Concepts of the Lithium Metal Anode in Solid-State Batteries. Chem. Rev. *120*, 7745–7794. https://doi.org/10.1021/acs.chemrev.0c00431.

11. Lee, Y.-G., Fujiki, S., Jung, C., Suzuki, N., Yashiro, N., Omoda, R., Ko, D.-S., Shiratsuchi, T., Sugimoto, T., Ryu, S., et al. (2020). High-Energy Long-Cycling All-Solid-State Lithium Metal Batteries Enabled By Silver–Carbon Composite Anodes. Nat. Energy *5*, 299–308. https://doi.org/10.1038/s41560-020-0575-z.

12. Shen, Y., Zhang, Y., Han, S., Wang, J., Peng, Z., and Chen, L. (2018). Unlocking the Energy Capabilities of Lithium Metal Electrode with Solid-State Electrolytes. Joule *2*, 1674–1689. https://doi.org/10.1016/j.joule.2018.06.021.

13. Janek, J., and Zeier, W.G. (2023). Challenges in Speeding up Solid-State Battery Development. Nat. Energy *8*, 230–240. https://doi.org/10.1038/s41560-023-01208-9.

14. Culver, S.P., Koerver, R., Krauskopf, T., and Zeier, W.G. (2018). Designing Ionic Conductors: The Interplay between Structural Phenomena and Interfaces in Thiophosphate-Based Solid-State Batteries. Chem. Mater. *30*, 4179–4192. https://doi.org/10.1021/acs.chemmater.8b01293.

15. Zhu, Y., He, X., and Mo, Y. (2015). Origin of Outstanding Stability in the Lithium Solid Electrolyte Materials: Insights from Thermodynamic Analyses Based on First-Principles Calculations. ACS Appl. Mater. Interfaces *7*, 23685–23693. https://doi.org/10.1021/acsami.5b07517.

16. Richards, W.D., Miara, L.J., Wang, Y., Kim, J.C., and Ceder, G. (2016). Interface Stability in Solid-State Batteries. Chem. Mater. *28*, 266–273. https://doi.org/10.1021/acs.chemmater.5b04082.

17. Hatzell, K.B., Chen, X.C., Cobb, C.L., Dasgupta, N.P., Dixit, M.B., Marbella, L.E., McDowell, M.T., Mukherjee, P.P., Verma, A., Viswanathan, V., et al. (2020). Challenges in Lithium Metal Anodes for Solid-State Batteries. ACS Energy Lett. *5*, 922–934. https://doi.org/10.1021/acsenergylett.9b02668.

18. Albertus, P., Anandan, V., Ban, C., Balsara, N., Belharouak, I., Buettner-Garrett, J., Chen, Z., Daniel, C., Doeff, M., Dudney, N.J., et al. (2021). Challenges for and Pathways toward Li-Metal-Based All-Solid-State Batteries. ACS Energy Lett. *6*, 1399–1404. https://doi.org/10.1021/acsenergylett.1c00445.

19. Wenzel, S., Sedlmaier, S.J., Dietrich, C., Zeier, W.G., and Janek, J. (2018). Interfacial Reactivity and Interphase Growth of Argyrodite Solid Electrolytes at Lithium Metal Electrodes. Solid State Ionics *318*, 102–112. https://doi.org/10.1016/j.ssi.2017.07.005.

20. Lee, C., Han, S.Y., Lewis, J.A., Shetty, P.P., Yeh, D., Liu, Y., Klein, E., Lee, H.-W., and McDowell, M.T. (2021). Stack Pressure Measurements to Probe the Evolution of the Lithium–Solid-State Electrolyte Interface. ACS Energy Lett. *6*, 3261–3269. https://doi.org/10.1021/acsenergylett.1c01395.

21. Wenzel, S., Leichtweiss, T., Krüger, D., Sann, J., and Janek, J. (2015). Interphase Formation on Lithium Solid Electrolytes—An in situ Approach to Study Interfacial Reactions by Photoelectron Spectroscopy. Solid State Ionics *278*, 98–105. https://doi.org/10.1016/j.ssi.2015.06.001.

22. Wenzel, S., Randau, S., Leichtweiß, T., Weber, D.A., Sann, J., Zeier, W.G., and Janek, J. (2016). Direct Observation of the Interfacial Instability of the Fast Ionic Conductor $Li_{10}GeP_2S_{12}$ at the Lithium Metal Anode. Chem. Mater. *28*, 2400–2407. https://doi.org/10.1021/acs.chemmater.6b00610.

23. Peled, E. (1979). The Electrochemical Behavior of Alkali and Alkaline Earth Metals in Nonaqueous Battery Systems—The Solid Electrolyte Interphase Model. J. Electrochem. Soc. *126*, 2047–2051. https://doi.org/10.1149/1.2128859.

24. Jagger, B., and Pasta, M. (2023). Solid Electrolyte Interphases in Lithium Metal Batteries. Joule *7*, 2228–2244. https://doi.org/10.1016/j.joule.2023.08.007.

25. Zhao, Q., Stalin, S., and Archer, L.A. (2021). Stabilizing Metal Battery Anodes through the Design of Solid Electrolyte Interphases. Joule *5*, 1119–1142. https://doi.org/10.1016/j.joule.2021.03.024.

26. Wenzel, S., and Justus Liebig University, Giessen. (2016). Thermodynamic and Kinetic Instability of Inorganic Solid Electrolytes at Lithium and Sodium Metal Electrodes (Universitätsbibliothek Gießen. JLUpub). https://doi.org/10.22029/jlupub-10375.

27. Riegger, L.M., Mittelsdorf, S., Fuchs, T., Rueß, R., Richter, F.H., and Janek, J. (2023). Evolution of the Interphase between Argyrodite-Based Solid Electrolytes and the Lithium Metal Anode—The Kinetics of Solid Electrolyte Interphase Growth. Chem. Mater. *35*, 5091–5099. https://doi.org/10.1021/acs.chemmater.3c00676.

28. Aktekin, B., Riegger, L.M., Otto, S.-K., Fuchs, T., Henss, A., and Janek, J. (2023). SEI Growth on Lithium Metal Anodes in Solid-State Batteries Quantified with Coulometric Titration Time Analysis. Nat. Commun. *14*, 6946. https://doi.org/10.1038/s41467-023-42512-y.

29. Otto, S.-K., Riegger, L.M., Fuchs, T., Kayser, S., Schweitzer, P., Burkhardt, S., Henss, A., and Janek, J. (2022). In Situ Investigation of Lithium Metal–Solid Electrolyte Anode Interfaces with ToF-SIMS. Adv. Materials. Inter. *9*, 2102387. https://doi.org/10.1002/admi.202102387.

30. Guo, R., Hobold, G.M., and Gallant, B.M. (2022). The Ionic Interphases of the Lithium Anode in Solid State Batteries. Curr. Opin. Solid State Mater. Sci. *26*, 100973. https://doi.org/10.1016/j.cossms.2021.100973.

31. Krauskopf, T., Dippel, R., Hartmann, H., Peppler, K., Mogwitz, B., Richter, F.H., Zeier, W.G., and Janek, J. (2019). Lithium-Metal Growth Kinetics on LLZO Garnet-Type Solid Electrolytes. Joule *3*, 2030–2049. https://doi.org/10.1016/j.joule.2019.06.013.

32. Wu, B., Wang, S., Lochala, J., Desrochers, D., Liu, B., Zhang, W., Yang, J., and Xiao, J. (2018). The Role of the Solid Electrolyte Interphase Layer in Preventing Li Dendrite Growth in Solid-State Batteries. Energy Environ. Sci. *11*, 1803–1810. https://doi.org/10.1039/C8EE00540K.

33. Xu, R., Cheng, X.-B., Yan, C., Zhang, X.-Q., Xiao, Y., Zhao, C.-Z., Huang, J.-Q., and Zhang, Q. (2019). Artificial Interphases for Highly Stable Lithium Metal Anode. Matter *1*, 317–344. https://doi.org/10.1016/j.matt.2019.05.016.

34. Hao, H., Liu, Y., Greene, S.M., Yang, G., Naik, K.G., Vishnugopi, B.S., Wang, Y., Celio, H., Dolocan, A., Tsai, W.-Y., et al. (2023). Tuned Reactivity at the Lithium Metal–Argyrodite Solid State Electrolyte Interphase. Adv. Energy Mater. *13*, 2301338. https://doi.org/10.1002/aenm.202301338.

35. Ye, L., Lu, Y., Wang, Y., Li, J., and Li, X. (2024). Fast Cycling of Lithium Metal in Solid-State Batteries by Constriction-Susceptible Anode materials. Nat. Mater. *23*, 244–251. https://doi.org/10.1038/s41563-023-01722-x.

36. Ye, L., and Li, X. (2021). A Dynamic Stability Design Strategy for Lithium Metal Solid State Batteries. Nature *593*, 218–222. https://doi.org/10.1038/s41586-021-03486-3.

37. Tan, D.H.S., Chen, Y.-T., Yang, H., Bao, W., Sreenarayanan, B., Doux, J.-M., Li, W., Lu, B., Ham, S.-Y., Sayahpour, B., et al. (2021). Carbon-free high-loading silicon anodes enabled by sulfide solid electrolytes. Science *373*, 1494–1499. https://doi.org/10.1126/science.abg7217.

38. Cheng, D., Wynn, T.A., Wang, X., Wang, S., Zhang, M., Shimizu, R., Bai, S., Nguyen, H., Fang, C., Kim, M., et al. (2020). Unveiling the Stable Nature of the Solid Electrolyte Interphase between Lithium Metal and LiPON via Cryogenic Electron Microscopy. Joule *4*, 2484–2500. https://doi.org/10.1016/j.joule.2020.08.013.

39. Gibson, J.S., Narayanan, S., Swallow, J.E.N., Kumar-Thakur, P., Pasta, M., Lee, T.-L., and Weatherup, R.S. (2022). Gently Does It!: in situ Preparation of Alkali Metal-Solid Electrolyte Interfaces for Photoelectron Spectroscopy. Faraday Discuss. *236*, 267–287. https://doi.org/10.1039/d1fd00118c.

40. Xu, Y., Jia, H., Gao, P., Galvez-Aranda, D.E., Beltran, S.P., Cao, X., Le, P.M.L., Liu, J., Engelhard, M.H., Li, S., et al. (2023). Direct in situ Measurements of Electrical Properties of Solid-Electrolyte Interphase on Lithium Metal Anodes. Nat. Energy *8*, 1345–1354. https://doi.org/10.1038/s41560-023-01361-1.

41. Luo, S., Liu, X., Zhang, X., Wang, X., Wang, Z., Zhang, Y., Wang, H., Ma, W., Zhu, L., and Zhang, X. (2022). Nanostructure of the Interphase Layer between a Single Li Dendrite and Sulfide Electrolyte in All-Solid-State Li

Batteries. ACS Energy Lett. *7*, 3064–3071. https://doi.org/10.1021/acsenergylett.2c01543.

42. Bron, P., Roling, B., and Dehnen, S. (2017). Impedance Characterization Reveals Mixed Conducting Interphases between Sulfidic Superionic Conductors and Lithium Metal Electrodes. J. Power Sources *352*, 127–134. https://doi.org/10.1016/j.jpowsour.2017.03.103.

43. Wagner, C. (1955). Thermodyn. Kinetics. In Proceedings 7th Meeting International Communications on Electrochemistry (Butterworth), p. 361.

44. Hebb, M.H. (1952). Electrical Conductivity of Silver Sulfide. J. Chem. Phys. *20*, 185–190. https://doi.org/10.1063/1.1700165.

45. Narayanan, S., Ulissi, U., Gibson, J.S., Chart, Y.A., Weatherup, R.S., and Pasta, M. (2022). Effect of Current Density on the Solid Electrolyte Interphase Formation at the Lithium|Li_6PS_5Cl Interface. Nat. Commun. *13*, 7237. https://doi.org/10.1038/s41467-022-34855-9.

46. Wenzel, S., Weber, D.A., Leichtweiss, T., Busche, M.R., Sann, J., and Janek, J. (2016). Interphase Formation and Degradation of Charge Transfer Kinetics between a Lithium Metal Anode and Highly Crystalline $Li_7P_3S_{11}$ Solid Electrolyte. Solid State Ionics *286*, 24–33. https://doi.org/10.1016/j.ssi.2015.11.034.

47. Marino, C., Boulet, L., Gaveau, P., Fraisse, B., and Monconduit, L. (2012). Nanoconfined Phosphorus in Mesoporous Carbon as an Electrode for Li-ion Batteries: Performance and Mechanism. J. Mater. Chem. *22*, 22713. https://doi.org/10.1039/c2jm34562e.

48. Park, C.-M., and Sohn, H.-J. (2007). Black Phosphorus and its Composite for Lithium Rechargeable Batteries. Adv. Mater. *19*, 2465–2468. https://doi.org/10.1002/adma.200602592.

49. Peng, C., Chen, H., Zhong, G., Tang, W., Xiang, Y., Liu, X., Yang, J., Lu, C., and Yang, Y. (2019). Capacity Fading induced by Phase Conversion Hysteresis within Alloying Phosphorus Anode. Nano Energy *58*, 560–567. https://doi.org/10.1016/j.nanoen.2019.01.035.

50. Finch, G.I., and Fordham, S. (1936). The Effect of Crystal-Size on Lattice-Dimensions. Proc. Phys. Soc. *48*, 85–94. https://doi.org/10.1088/0959-5309/48/1/312.

51. Kubel, F., Bertheville, B., and Bill, H. (1999). Crystal structure of dilithiumsulfide, Li_2S. Z. Kristallogr. New Cryst. Struct. *214*, 302. https://doi.org/10.1515/ncrs-1999-0303.

52. Aktekin, B., Kataev, E., Riegger, L.M., Garcia-Diez, R., Chalkley, Z., Becker, J., Wilks, R.G., Henss, A., Bär, M., and Janek, J. (2024). Operando Photoelectron Spectroscopy Analysis of Li_6PS_5Cl Electrochemical Decomposition Reactions in Solid-State Batteries. ACS Energy Lett. *9*, 3492–3500. https://doi.org/10.1021/acsenergylett.4c01072.

53. Rayavarapu, P.R., Sharma, N., Peterson, V.K., and Adams, S. (2012). Variation in Structure and Li^+-Ion Migration in Argyrodite-type Li_6PS_5X (X = Cl, Br, I) solid electrolytes. J. Solid State Electrochem. *16*, 1807–1813. https://doi.org/10.1007/s10008-011-1572-8.

54. Kraft, M.A., Culver, S.P., Calderon, M., Böcher, F., Krauskopf, T., Senyshyn, A., Dietrich, C., Zevalkink, A., Janek, J., and Zeier, W.G. (2017). Influence of Lattice Polarizability on the Ionic Conductivity in the Lithium Superionic Argyrodites Li_6PS_5X (X = Cl, Br, I). J. Am. Chem. Soc. *139*, 10909–10918. https://doi.org/10.1021/jacs.7b06327.

55. Boulineau, S., Courty, M., Tarascon, J.-M., and Viallet, V. (2012). Mechanochemical Synthesis of Li-Argyrodite Li_6PS_5X (X=Cl, Br, I) as Sulfur-Based Solid Electrolytes for All Solid State Batteries Application. Solid State Ionics *221*, 1–5. https://doi.org/10.1016/j.ssi.2012.06.008.

56. Zhou, L., Park, K.-H., Sun, X., Lalère, F., Adermann, T., Hartmann, P., and Nazar, L.F. (2019). Solvent-Engineered Design of Argyrodite Li_6PS_5X (X = Cl, Br, I) Solid Electrolytes with High Ionic Conductivity. ACS Energy Lett. *4*, 265–270. https://doi.org/10.1021/acsenergylett.8b01997.

57. Heo, Y.J., Seo, S.-D., Hwang, S.-H., Choi, S.H., and Kim, D.-W. (2022). One-Pot Aprotic Solvent-Enabled Synthesis of Superionic Li-Argyrodite Solid Electrolyte. Int. J. Energy Res. *46*, 17644–17653. https://doi.org/10.1002/er.8324.

58. Deiseroth, H.-J., Maier, J., Weichert, K., Nickel, V., Kong, S.-T., and Reiner, C. (2011). Li_7PS_6 and Li_6PS_5X (X: Cl, Br, I): Possible Three-dimensional Diffusion Pathways for Lithium Ions and Temperature Dependence of the Ionic Conductivity by Impedance Measurements. Zeitschrift anorg. allg. Chem. *637*, 1287–1294. https://doi.org/10.1002/zaac.201100158.

59. Lorger, S., Usiskin, R.E., and Maier, J. (2019). Transport and Charge Carrier Chemistry in Lithium Sulfide. Adv. Funct. Materials *29*, 1807688. https://doi.org/10.1002/adfm.201807688.

60. Lorger, S., Narita, K., Usiskin, R., and Maier, J. (2021). Enhanced Ion Transport in Li_2O and Li_2S Films. Chem. Commun. (Camb) *57*, 6503–6506. https://doi.org/10.1039/d1cc00557j.

61. Zhang, K., Wang, L., Hu, Z., Cheng, F., and Chen, J. (2014). Ultrasmall Li_2S Nanoparticles Anchored in Graphene Nanosheets for High-Energy Lithium-Ion Batteries. Sci. Rep. *4*, 6467. https://doi.org/10.1038/srep06467.

62. Nazri, G. (1989). Preparation, Structure and Ionic Conductivity of Lithium Phosphide. Solid State Ionics *34*, 97–102. https://doi.org/10.1016/0167-2738(89)90438-4.

63. Maltsev, A.P., Chepkasov, I.V., Kvashnin, A.G., and Oganov, A.R. (2023). Ionic Conductivity of Lithium Phosphides. Crystals *13*, 756. https://doi.org/10.3390/cryst13050756.

64. Li, J., Liu, D., Sun, H., Qu, D., Xie, Z., Tang, H., and Liu, J. (2023). Mixed Ion-Electron Conducting Li_3P for Efficient Cathode Prelithiation of All-Solid-State Li-Ion Batteries. Smartmat. *4*, e1200. https://doi.org/10.1002/smm2.1200.

65. Sharon, M., and Pradhananga, R.R. (1981). Ionic Conductivity of Pure and Ca_{2+}- and Sr_{2+}-Doped Single Crystals of LiCl. J. Solid State Chem. *40*, 20–27. https://doi.org/10.1016/0022-4596(81)90355-8.

66. Armstrong, R.D., and Landles, K. (1982). Lithium Ion Conducting Solids for Ambient Applications. J. Appl. Electrochem. *12*, 533–535. https://doi.org/10.1007/BF00614979.

67. Mercier, R., Tachez, M., Malugani, J.P., and Robert, G. (1985). Effect of Homovalent (I_-—Br_-) Ion Substitution on the Ionic Conductivity of LiI_{1-x} Br_x Systems. Solid State Ionics *15*, 109–112. https://doi.org/10.1016/0167-2738(85)90088-8.

68. Poulsen, F.W. (1981). Ionic Conductivity of Solid Lithium Iodide and its Monohydrate. Solid State Ionics *2*, 53–57. https://doi.org/10.1016/0167-2738(81)90020-5.

69. Jackson, B.J.H., and Young, D.A. (1969). Ionic Conduction in Pure and Doped Single-Crystalline Lithium Iodide. J. Phys. Chem. Solids *30*, 1973–1976. https://doi.org/10.1016/0022-3697(69)90174-7.

70. Schmalzried, H. (1995). Chemical Kinetics of Solids (Wiley-VCH Press).

71. Wenzel, S., Leichtweiss, T., Weber, D.A., Sann, J., Zeier, W.G., and Janek, J. (2016). Interfacial Reactivity Benchmarking of the Sodium Ion Conductors Na_3PS_4 and Sodium β-Alumina for Protected Sodium Metal Anodes and Sodium All-Solid-State Batteries. ACS Appl. Mater. Interfaces *8*, 28216–28224. https://doi.org/10.1021/acsami.6b10119.

72. Li, Y., Canepa, P., and Gorai, P. (2022). Role of Electronic Passivation in Stabilizing the Lithium- $Li_xPO_yN_z$ Solid-Electrolyte Interphase. PRX Energy *1*, 023004. https://doi.org/10.1103/PRXEnergy.1.023004.

73. Le Van-Jodin, L., Ducroquet, F., Sabary, F., and Chevalier, I. (2013). Dielectric Properties, Conductivity and Li+ Ion Motion in LiPON Thin Films. Solid State Ionics *253*, 151–156. https://doi.org/10.1016/j.ssi.2013.09.031.

74. Su, Y., Falgenhauer, J., Polity, A., Leichtweiß, T., Kronenberger, A., Obel, J., Zhou, S., Schlettwein, D., Janek, J., and Meyer, B.K. (2015). LiPON Thin Films with High Nitrogen Content for Application in Lithium Batteries and Electrochromic Devices Prepared by RF Magnetron Sputtering. Solid State Ionics *282*, 63–69. https://doi.org/10.1016/j.ssi.2015.09.022.

75. Li, J., Dudney, N.J., Nanda, J., and Liang, C. (2014). Artificial Solid Electrolyte Interphase To Address the Electrochemical Degradation of Silicon Electrodes. ACS Appl. Mater. Interfaces *6*, 10083–10088. https://doi.org/10.1021/am5009419.

76. Eckhardt, J.K., Fuchs, T., Burkhardt, S., Klar, P.J., Janek, J., and Heiliger, C. (2023). Guidelines for Impedance Analysis of Parent Metal Anodes in Solid-State Batteries and the Role of Current Constriction at Interface Voids, Heterogeneities, and SEI. Adv. Materials Inter. *10*, 2202354. https://doi.org/10.1002/admi.202202354.

77. Landgraf, V., Tu, M., Cheng, Z., de Leeuw, J., Ganapathy, S., Wagemaker, M., and Famprikis, T. (2023). Entropy-Induced High Conductivity in Fully-Reduced Electrolytes for Solid-State Batteries with Lithium Metal Anodes. Preprint at ChemRxiv.

78. Landgraf, V., Famprikis, T., de Leeuw, J., Bannenberg, L.J., Ganapathy, S., and Wagemaker, M. (2023). Li_5NCl_2: A Fully-Reduced, Highly-Disordered Nitride-Halide Electrolyte for Solid-State Batteries with Lithium-Metal Anodes. ACS Appl. Energy Mater. *6*, 1661–1672. https://doi.org/10.1021/acsaem.2c03551.

79. Kolesnikov, A., Wulfers, T., Kolek, M., Bieker, P., Stan, M.C., and Winter, M. (2022). Lithium Powder Synthesis and Preparation of Powder-Based Composite Electrodes for Application in Lithium Metal Batteries. Energy Tech. *10*, 2100871. https://doi.org/10.1002/ente.202100871.

80. Coelho, A.A. (2018). TOPAS and TOPAS-Academic: An Optimization Program Integrating Computer Algebra and Crystallographic Objects Written in C++. J. Appl. Crystallogr. *51*, 210–218. https://doi.org/10.1107/S1600576718000183.

81. jEdit v4.3. http://www.jedit.org/index.php.

82. Santhosha, A.L., Medenbach, L., Buchheim, J.R., and Adelhelm, P. (2019). The Indium–Lithium Electrode in Solid-State Lithium-Ion Batteries: Phase Formation, Redox Potentials, and Interface Stability. Batteries Supercaps *2*, 524–529. https://doi.org/10.1002/batt.201800149.